HHS Public Access

Author manuscript

Magn Reson Med. Author manuscript; available in PMC 2017 October 01.

Published in final edited form as:

Magn Reson Med. 2016 October ; 76(4): 1325–1334. doi:10.1002/mrm.26017.

A Flexible Nested Sodium and Proton Coil Array with Wideband Matching for Knee Cartilage MRI at 3 Tesla

Ryan Brown[1,2,3], **Karthik Lakshmanan**[1,2], **Guillaume Madelin**[1,2], **Leeor Alon**[1,2,3], **Gregory Chang**[1,2], **Daniel K. Sodickson**[1,2,3], **Ravinder R. Regatte**[1,2], and **Graham C. Wiggins**[1,2]

[1]Bernard and Irene Schwartz Center for Biomedical Imaging, Department of Radiology, New York University School of Medicine, New York, NY USA

[2]Center for Advanced Imaging Innovation and Research (CAI[2]R), Department of Radiology, New York University School of Medicine, New York, NY USA

[3]NYU WIRELESS, Polytechnic Institute of New York University, 2 Metro Tech Center, Brooklyn, NY, 11201

Abstract

Purpose—We describe a 6×2 channel sodium/proton array for knee MRI at 3 Tesla. Multi-element coil arrays are desirable because of well-known signal-to-noise ratio advantages over volume and single-element coils. However, low coil-tissue coupling that is characteristic of coils operating at low frequency can make the potential gains from a phased array difficult to realize.

Methods—The issue of low coil-tissue coupling in the developed six channel sodium receive array was addressed by implementing 1) a mechanically flexible former to minimize coil-to-tissue distance and reduce the overall diameter of the array and 2) a wideband matching scheme that counteracts preamplifier noise degradation caused by coil coupling and a high quality factor. The sodium array was complemented with a nested proton array to enable standard MRI.

Results—The wideband matching scheme and tight-fitting mechanical design contributed to greater than 30% central SNR gain on the sodium module over a mono-nuclear sodium birdcage coil, while the performance of the proton module was sufficient for clinical imaging.

Conclusion—We expect the strategies presented in this work to be generally relevant in high density receive arrays, particularly in x-nuclei or small animal applications, or in those where the array is distant from the targeted tissue.

Keywords

dual-tuned; phased-array; FLORET; preamplifier noise; coupling

Corresponding Author: Ryan Brown, Ph.D., Bernard and Irene Schwartz Center for Biomedical Imaging, New York University School of Medicine, 660 First Avenue, Room 401, New York, NY, Tel: 212-263-3396, Fax: 212-263-7541, ryan.brown@nyumc.org.

INTRODUCTION

Quantitative sodium MRI is a non-invasive technique that is highly specific to the glycosaminoglycan (GAG) content (1,2) in knee cartilage and can be used as a means of detection and assessment of the degree of biochemical degradation in osteoarthritis (OA) (3,4). One of the fundamental challenges in sodium MRI is the relatively low sensitivity due to low sodium concentration in the body. In healthy cartilage, the average sodium concentration is generally in the range 200-300 mmol/L, which is around 260-400 times lower than the in vivo water proton concentration (5). This is compounded by low sodium receptivity (which is associated with a low gyromagnetic ratio that causes both reduced polarization and lower coil sensitivity). These factors result in a sodium MRI signal that is approximately 3000-4500 times lower than the proton signal in cartilage. These inherent disadvantages in sodium MRI can result in undesirable compromises in spatial resolution that can be unacceptable for cartilage visualization as well as long examination times that make it difficult to combine both proton and sodium knee imaging into a single protocol. Efficient pulse sequences and advanced reconstruction techniques have recently been developed to help alleviate these limitations (6-12). Further signal-to-noise ratio (SNR) enhancement can be achieved with optimized radiofrequency coils. Recently, dual-nuclei coil development has seen a shift from volume (13-22) and single-channel surface (23-30) to multi-channel phased arrays (31-37), which coincides with a renewed interest in “x-nuclei” or “low gamma” applications. While the advantages of proton multi-channel arrays have been well documented, sodium arrays have been less developed due to their role as a research, rather than clinical, tool.

Along with the promise for SNR gain from a multi-channel array come engineering challenges that arise in a low gamma regime in which low tissue-coil coupling can result in an unfavorable noise balance and degrade expected performance advantages over a traditional volume coil. Low tissue-coil coupling in a phased array has the additional disadvantage of accentuating preamplifier noise coupling, where noise generated in the transistor projects into the coil and is transferred to other elements via their mutual impedance (38-44). While this effect is generally ignored in proton arrays where high tissue-coil coupling and hence a reduced quality factor diminish its significance, SNR degradation can be substantial when inductive coupling to the tissue is low and/or high coil coupling conditions are present. In this work, we detail the design strategy in a multi-channel sodium and proton knee coil that counteracts low coil-tissue coupling on the sodium module by implementing a wideband matching scheme and a mechanically flexible former (45). We further tackle the challenge of providing proton imaging capability in the ensemble array without substantially compromising the performance of the sodium module.

METHODS

Coil Overview

The dual-nuclei sodium/proton knee array can be divided into three functional modules: 1) a high-pass birdcage coil for sodium transmission was built on the outer housing layer, which was divisible into anterior and posterior sections for patient entry, 2) a six-channel array for sodium reception was built on the inner layer, and 3) a six-channel array for proton

transmission and reception, whose elements were nested within the sodium array, was also built on the inner layer. The schematic diagram and photographs in Figure 1 and Figure 2 illustrate this arrangement. More details are given on each module in the following sections.

Sodium Receive Array

High performance of the sodium receive module was the key design criteria for the ensemble sodium/proton array. Two strategies were implemented to improve sodium sensitivity, which distinguish the proposed 3T dual-nuclei sodium/proton knee coil from conventional dual-nuclei knee coils: 1) a mechanically flexible housing system and 2) wideband matching. First, the sodium receive array was designed to minimize coil-tissue distance and reduce the allowable former diameter, both of which can be expected to improve SNR over rigid designs. Whereas rigid knee coils typically require ~18 to 21 cm diameter to accommodate a range of patient sizes, the proposed coil was built on flexible housing that allowed its nominal diameter to be reduced to 15 cm without compromising accessibility. This strategy helped counteract the low coil-tissue coupling that is characteristic of coils operating at a low resonance frequency (in this case 32.6 MHz). The flexible housing consisted of six rigid modules linked together by five hinges built in-house whose axes were along the z-axis. A discontinuity between two coils allowed the array to be opened and wrapped around the knee for subject positioning. Given the interest in patellar cartilage in the anterior region of the knee, the discontinuity was chosen to be at the posterior position (between coils 1 and 6 in Figure 1). The rationale was that the posterior coil gap required to accommodate large subjects would not affect performance in the anterior region. The coil count of six [7.9 cm (arc length) × 15 cm (head/foot)] was selected empirically based on target unloaded-to-loaded quality factor (Q) ratio of two and desired head/foot coverage of roughly 12 cm. Coils were built using 3 mm diameter copper tubing built onto FR4 circuit board, which have favorable shielding and resistance properties compared to flat copper traces (46,47). Neighboring coils were decoupled by choosing the appropriate value for the capacitance in their shared legs (48).

To maximize array performance in a regime where the operating frequency is low and coil coupling can be high, preamplifier noise coupling should be considered. In this phenomenon, noise generated in a given preamplifier is projected into the associated coil and further transferred to other coils in the array (38,40,41,43). The additional noise appears on the diagonal elements of the correlation matrix and therefore cannot be counteracted by decorrelation or matched filter image reconstruction techniques (38). Preamplifier noise coupling is a function of the noise figure of the preamplifier itself, match conditions, the normalized magnetic coupling coefficient (defined as the ratio of the width of the split resonance frequency in a two-coil system and the resonance frequency of an isolated coil $k = \Delta f/f_0$), and the coil Q. Small coil elements operating at low frequencies result in poor tissue-coil coupling, which is associated with high Q values and preamplifier noise coupling, as will become clear in the following section. Note that this noise source is routinely and appropriately ignored in typical clinical proton applications where the coil Q and coil interaction are both low due to heavy coupling to the sample and the use of decoupling strategies (geometrical overlapping, capacitive decoupling, etc.).

A detailed theoretical outline of noise coupling and its mitigation through wideband matching has been given by Vester et al (43). We focus on the application of the technique in this section. The effective noise factor of a preamplifier in a two-coil system is

$$F' = F \cdot \left(\frac{1}{2z} + \frac{z}{2} + \frac{(kQ)^2}{2z} \right), \quad [1]$$

where F is the noise factor of the isolated preamplifier in linear units and z is the impedance transformation ratio that defines the ratio of the impedance required for a classic noise match (commonly 50 Ω) to that presented by the coil at the preamplifier input. The classic match strategy implies $z = 1$ and the effective added noise factor from Eq.[1] is $F_c' = F \cdot \left[1 + (kQ)^2/2 \right]$. The optimal impedance transformation ratio under the wideband match strategy is

$$z = |1 + jkQ|, \quad [2]$$

which reduces Eq. [1] to $F_w' = F \cdot \sqrt{1 + (kQ)^2}$. The additional noise factor can be related to the SNR by recognizing $SNR \propto 1 \sqrt{1 + F'}$, where unity represents the baseline noise from sources such as the subject and coil and the square root accounts for the measurement of voltage SNR in MRI. Given that F' reduces to F when coil coupling is not present ($k = 0$) and a classic match is implemented (z = 1), the ratio of SNR without preamplifier noise coupling to that with coupling follows as

$$\eta = \sqrt{1 + F} / \sqrt{1 + F'}. \quad [3]$$

Figure 3 shows the predicted normalized SNR values of a coil element in a two-channel array matched using the classic and wideband match strategies, along with the optimal reflection coefficient for a range of kQ values. The reflection coefficient for optimal wideband matching is determined by converting the impedance transformation ratio given in Eq. [2]: $S_{11}^w = (z \cdot Z_0 - Z_0) / (z \cdot Z_0 + Z_0)$, where Z_0 = 50Ω is the impedance corresponding to the classic match.

In the developed array, preamplifier noise coupling was exacerbated between coils 1 and 6, whose close proximity but lack of a decoupling mechanism was a design choice required to accommodate the mechanically flexible housing. With the housing in its nominal position, the magnetic coupling coefficient was measured using a double probe by dividing the resonance frequency of a given coil (measured with all other coils open-circuited) by the difference in resonance frequencies between two coupled modes (measured with all but two coils open circuited). The coupling coefficients were: $k = 0.12$ for gapped coils 1 and 6, $k = 0.03$ for next-nearest neighbor pairs (coils 1 and 3, 2 and 4, 3 and 5, and 4 and 6), and $k \approx 0$ for capacitively decoupled pairs (coils 1 and 2, 2 and 3, 3 and 4, 4 and 5, and 5 and 6). The

Q was approximately 95 when loaded with a 1.9 L water phantom doped with [NaCl] = 46.8mM (5.2 g) and [$NiSO_4$] = 18.4mM (5.4 g) to approximate knee loading. Inserting the appropriate values into Eq. [2] gives $|z| = 11.4$ for coils 1 and 6, and 3.1 for all other coils. To apply wideband matching in these conditions, $|S_{11}|$ was set to 0.84 for coils 1 and 6, and to 0.51 for all other coils by making appropriate adjustments to the capacitor values (Figure 4). The match strategies were compared through SNR measurements in a phantom with the array matched using the wideband scheme and the classic scheme where $|S_{11}|$ was adjusted to zero in all coils as illustrated in the Smith Chart traces in Figure 5. In both experiments, the phase lengths between the sodium preamplifiers and receive coils was adjusted to achieve preamplifier decoupling (49).

After tuning and matching the sodium receive coils as described above, an active detuning circuit was added to each element to avoid RF field distortion during sodium excitation. With the detuning circuits tuned to the sodium frequency and positioned at each of the coil drive ports, an undesirable resonance mode near the proton frequency was observed when the circuits were forward biased. In light of this, the positions of the detuning circuits were alternated between the coil port and the capacitor position on the opposite side of the coil element, which provided the requisite detuning at the sodium frequency and did not produce a resonant mode near the proton frequency. Supplementary protection was provided by a fuse rated to 700 mA.

Detunable Sodium Birdcage

A concentric detunable sodium birdcage coil was installed to provide a homogeneous transmit field. An eight-rung high-pass birdcage was used because its uniform imaging mode and non-uniform high-order modes occur at frequencies well below the proton resonant frequency thus reducing the likelihood of birdcage and proton mode interaction. Full-wave simulations using a current mode expansion with Dyadic Green's functions (50,51) were used to guide the choice of birdcage dimensions using methods similar to those previously described (32). The selected birdcage dimensions (25 cm diameter × 15 cm length) were based on tradeoffs between high B_1^+ uniformity that necessitates a larger length-to-diameter ratio and high peak B_1^+ that calls for small diameter and smaller length-to-diameter ratio. Another requirement was that the birdcage fit around the sodium receive array in a concentric manner with minimal disturbance to the contralateral leg. In practice, the birdcage was tuned during sodium transmission and detuned during sodium reception and proton operation by appropriately biasing PIN diodes that were in series with each rung. The birdcage was physically divided into anterior and posterior half-cylinders in order to allow convenient patient positioning. Coaxial connectors provided robust electrical continuity between the two halves (part numbers 122-124-003-257-001 [female] and 122-124-004-257-001 [male], Odu-USA, Inc., Camarillo, CA).

Proton Transmit-Receive Array

The aim of the proton module was to provide anatomical imaging capability and static field shim analysis with minimal disturbance to the sodium receive array. This was accomplished using a nested strategy that has been previously demonstrated in various forms in which co-planar and concentric proton coils are added to the sodium array (26,27,29,32,33,52).

Specifically, an array of six transceive proton coils was constructed. Coil dimensions of 3.2 cm (arc length) × 10 cm (head/foot) were empirically selected base coverage and uniformity of large coils and tolerable coupling offered by small coils.

Neighboring proton coils were coupled by less than −11 dB (next-nearest neighbors were coupled by < −22 dB) owing to their relatively small geometry, gapped structure, and shielding provided by the surrounding concentric sodium elements. The pertinent values for wideband match calculations were $Q = 130$ and $k = 0.01$. Although Eq. [2] indicated an optimal wideband match with $z = 1.64$, Eq. [3] predicted a negligible (1%) SNR difference between the wideband and classic strategy. Further, since the proton coils were to be operated in transceive mode, a 50 Ω match was implemented for optimal transmit efficiency. To assess the impact of the proton coils on the sodium elements and vice versa, Q measurements were recorded on both sets of coils with the other set in both active and deactivated (open circuited) states.

The proton array was driven through a cascade of Wilkinson splitters (a 1:3 splitter followed by two 1:2 splitters, which is represented as a 1:6 splitter in Figure 6) that divided the power into six equal parts, whose outputs were fed to a set of six transmit/receive switches. To generate a circular polarized magnetic field, a phase shift equal to each coil's azimuthal position was built-in using appropriate lumped element phase shifters and coaxial cable segments.

Transmission Power Limits

To restrict tissue heating caused by the electric field of the proton transmit array, specific absorption rate (SAR) limits were set in accordance with those established by the International Electrotechnical Commission (IEC) (International Standard IEC 60601-2-33 2010). Local SAR was determined experimentally using methods similar to those described by Brown et al. (53). Briefly, the relative temperature change was measured in a homogeneous nonperfused cylindrical gelatin phantom composed of water doped with salt and sugar (54) such that its dielectric properties (conductivity = 0.64 S/m and relative permittivity = 65) were similar to those of muscle tissue (55). Proton gradient echo phase images were acquired before and after the application of a predetermined level of RF power. Oil phantoms were placed adjacent to the phantom to provide temperature insensitive phase references. Temperature change was determined using the proton resonance frequency shift method (56) and subsequently converted to SAR by applying $SAR(\vec{r}) = c \cdot \Delta T(\vec{r}) / \tau$, where $c = 2.5$ kJ kg^{-1} K^{-1} is the heat capacity of the phantom (measured using a KD2 probe; Decagon Devices, Inc, Pullman, WA), $\Delta T(\vec{r})$ is the local temperature change, and τ is the duration of the RF application. Note that the measurement was performed with the proton array in its nominal mechanical position. Given the mechanically flexible nature of the array, it is conceivable that the worst-case scenario in terms of constructive electric field interference was not reached. To account for this variable and other measurement inaccuracies, a two-fold safety margin was incorporated over the 20 W/kg local limit in the extremities set by the IEC and thus the proton time-averaged amplifier output was restricted to 37.6 W to establish a local SAR limit of 10 W/kg over a 360-second averaging period.

The sodium power limit was explored using an analogous procedure wherein the tissue-equivalent gel phantom was exposed to RF at 32.6 MHz. In this experiment, 24.4 W delivered for 604 s resulted in negligible heating (< 0.2 °C). No signs of reflected power, coil instability, or arcing were found, which could have potentially explained the lack of heating. Alternatively, the following rationale was used to determine the RF power limit. Assuming that the minimum volume of the extremity that will be exposed to RF is 0.68 L (57) with an estimated mass of 1 kg, the power limit is given by 10 W/ kg * 1 kg = 10 W. Accounting for the sodium transmit coil efficiency ($1 - Q_{loaded} / Q_{empty} = 0.38$), the time averaged power was limited to 10 W / 0.38 = 26.3 W, which is likely very conservative (only slightly above 24.4 W that resulted in no heating).

Imaging

Phantom and in vivo knee measurements were performed on a whole-body 3 Tesla scanner with multi-nuclear capability (TIM Trio, Siemens Healthcare, Erlangen, Germany) upon approval by our local IRB and with informed written consent from participants. The developed dual-nuclei array was compared to three single-nuclei coils available at our center: 1) sodium birdcage with 20 cm diameter × 17 cm length; 2) clinical proton knee coil with a birdcage transmitter and 15 channel receive array [approximately 18 cm diameter × 16.7 cm length, Quality Electrodynamics, Mayville, OH (58)]; and 3) clinical proton knee birdcage coil (approximately 21 cm diameter × 15 cm length, Invivo Corp., Gainesville, FL). Raw SNR measurements for both proton and sodium were made using a two-dimensional GRE pulse sequence in which images were acquired with and without RF excitation and processed using the method described by Kellman and McVeigh (59) (imaging parameters are listed in Table 1). Proton SNR is reported as $SNR = SNR_{raw}/\sin(FA)$, where FA is the flip angle measured using the method described by Fautz et al (60). Sodium B_1^+ maps were generated by acquiring a series of gradient echo images over a range of pulse amplitudes, fitting the signal intensities to a sine curve, and scaling its period by the appropriate factors. Metabolic and anatomical imaging was demonstrated using three-dimensional non-Cartesian Fermat looped orthogonally encoded trajectories (FLORET) and fast spin echo (FSE) acquisitions (6,8).

RESULTS

Sodium

The sodium receive coils had Q values of approximately 195 in isolation and 105 when loaded with a human leg. The sodium coil Q values changed by less than 5% when the proton coils were open-circuited, illustrating their low level of interaction.

Compared to the conventionally matched sodium array, the wideband match scheme provided a SNR gain of 10% in the center of the phantom and 50% in the posterior, which corresponded to the region covered by coils 1 and 6 (Figure 7a). The central SNR gain is in good agreement with Eq. [3], which predicts $\eta = 1.09$ for coils 3 to 5 (with $F = 1.122$), while that measured near posterior was less than the predicted gain ($\eta = 1.94$ for coils 1 and 6).

The developed dual-nuclei array provided a 30% SNR gain over the mono-nuclear sodium birdcage in the center and greater than two-fold in the periphery. The higher central SNR for the dual-nuclei array can be attributed to the smaller overall dimensions and close-fitting nature of the coil compared to the birdcage. Sodium imaging using the FLORET pulse sequence showed similar qualitative advantages (Figure 7b). FLORET SNR was not calculated due to the complex nature of the sampling scheme and image reconstruction algorithm.

In the phantom, B_1^+ uniformity of the sodium module was 96% in the central transverse slice of the knee phantom with the proposed coil (where uniformity was defined as one minus the standard deviation of the flip angle divided by its mean). In vivo transmit efficiency for both the constructed coil and mono-nuclear birdcage was 222 nT/V (corresponding to a 180° excitation with a 200 V hard pulse with 1 ms duration).

Proton

The proton coils had Q values of approximately 225 when unloaded and 130 when loaded by a human knee with the sodium coils resonant. The Q values were 235 (unloaded) and 100 (loaded) when the sodium coils were open circuited. In vivo transmit efficiency in the center of the knee was 91 nT/V and 100 nT/v for the constructed coil and mono-nuclear 15 channel array, respectively (corresponding to a 180° excitation with a 129 and 117 V hard pulse with 1 ms duration) (Figure 8a). Central SNR provided by the dual-nuclei array was 67% of that provided by the 15 channel mono-nuclear array (Figure 8b). The sparse local coils expectedly caused local B_1^+ hot spots in the posterior knee, and limited coverage was observed in the head-foot direction; the full width at half maximum length of the B_1^+ profile was 6.7 cm for the dual-nuclei array compared to 15.5 cm for the 15 channel mono-nuclear array. Nonetheless, coverage and central transmit uniformity provided by the developed array was adequate for PDw FSE imaging (Figure 8c). Additionally, the proton array provided a 15% SNR advantage in the center of a phantom over a traditional single-tuned knee birdcage coil.

DISCUSSION AND CONCLUSIONS

At frequencies as low as 32.6 MHz tissue losses are small and the resulting low unloaded to loaded Q ratio can make the potential gains from a phased array difficult to realize. This issue was addressed by implementing a wideband matching scheme and a mechanically flexible former to minimize coil to tissue distance and reduce the overall diameter of the array. The resulting dual-nuclei array provided substantial SNR gain in articular cartilage regions compared to a mono-nuclear sodium birdcage coil. The wideband matching scheme provided additional gain over the conventionally matched sodium array, where preamplifier noise coupling is accentuated due to coil coupling inherent in the mechanically flexible design and a characteristically high loaded Q-factor. We expect the wideband match strategy to be broadly relevant in high density receive arrays, particularly when the loaded coil quality factor is high as can be the case in x-nuclei or small animal applications, or in those where the array is distant from the targeted tissue (61).

Note that the broadband match calculations were simplified to that of a two-coil array wherein a given coil was considered to be coupled exclusively to one other coil. An eigenmode analysis that accounts for all coupling combinations may produce more favorable match conditions and help explain the deviation between the expected and measured results.

Coil sensitivity correction, along with those related to B_0 inhomogeneity and partial volume effects (62,63) may be critical for accurate sodium quantification in the cartilage. Although the multi-channel array improves SNR over a volume coil, its spatially varying sensitivity can make sodium quantification less straightforward. So-called “phantom replacement” and similar methods (64-66) that utilize phantom images to relate signal intensity to sodium concentration may not be sufficient due to the coil's flexible nature and therefore subject-dependent sensitivity. One way to address the issue is to estimate subject-specific individual coil sensitivity maps from the ratio between images acquired using the array and those acquired with the birdcage (assuming that the birdcage provides a homogeneous receive pattern), or directly from low-frequency k-space data already obtained in an array acquisition. Alternatively, computer simulations could be utilized to generate sensitivity maps over a range of coil positions and subsequently matched to that in the experiment. Low-resolution sensitivity maps could then be combined using a matched filter approach and finally applied to convert the high-resolution sodium image to standard units.

To maximize performance on the sodium module, some compromises were made to the proton module. The compromises were evident in the central SNR, which was lower than that provided by the 15 channel mono-nuclear proton receive array. This suggests that the gapped structure and counter-rotating proton currents generated in the sodium array combine to reduce performance below the optimal level. One way to alleviate out-of-phase currents is to install proton blocking trap circuits that have been demonstrated to minimally compromise x-nuclei performance (30,67). Nonetheless, proton SNR was 15% better than a mono-nuclear knee birdcage, suggesting that the proposed design is more favorable than standard “trap-based” dual-nuclei coils where the efficiency of the high-frequency channel is generally sacrificed by approximately one-half (23). Finally, the gapped proton design resulted in compromised transmit uniformity, which was considered a reasonable trade-off given the sodium SNR priority and the desire to avoid shielding the proton coils from the tissue by the low-impedance sodium coils. We also note that proton uniformity may be further compromised due to non-optimal phase offsets when the former is flexed.

In summary, we have laid out a blueprint for a sodium/proton array for knee cartilage MRI at 3 Tesla that can be translated to applications with similar tissue loading conditions. The sodium array provided at least 30% SNR gain over a mono-nuclear sodium birdcage coil, while proton channel performance was sufficient for clinical imaging. The design included a mechanically flexible sodium array and wideband matching strategy, which were both straightforward to implement. These features will help overcome low sodium MR sensitivity and improve GAG quantification in OA studies.

Acknowledgements

The authors thank Markus Vester for valuable discussions on wideband matching. Cornel Stefanescu is acknowledged for constructing the coil housing and Riccardo Lattanzi for providing the Dyadic Green's functions

code. This work was supported in part by National Institutes of Health grants R01AR067156-01, R01EB002568-07A1, and R03AR065763, and was performed under the rubric of the Center for Advanced Imaging Innovation and Research (CAI^{2}R, www.cai2r.net), a NIBIB Biomedical Technology Resource Center (NIH P41 EB017183).

References

1. Borthakur A, Mellon E, Niyogi S, Witschey W, Kneeland JB, Reddy R. Sodium and T1rho MRI for molecular and diagnostic imaging of articular cartilage. NMR Biomed. 2006; 19(7):781–821. [PubMed: 17075961]
2. Borthakur A, Shapiro EM, Beers J, Kudchodkar S, Kneeland JB, Reddy R. Sensitivity of MRI to proteoglycan depletion in cartilage: comparison of sodium and proton MRI. Osteoarthritis Cartilage. 2000; 8(4):288–293. [PubMed: 10903883]
3. Reddy R, Insko EK, Noyszewski EA, Dandora R, Kneeland JB, Leigh JS. Sodium MRI of human articular cartilage in vivo. Magn Reson Med. 1998; 39(5):697–701. [PubMed: 9581599]
4. Madelin G, Babb J, Xia D, Chang G, Krasnokutsky S, Abramson SB, Jerschow A, Regatte RR. Articular cartilage: evaluation with fluid-suppressed 7.0-T sodium MR imaging in subjects with and subjects without osteoarthritis. Radiology. 2013; 268(2):481–491. [PubMed: 23468572]
5. Madelin G, Regatte RR. Biomedical applications of sodium MRI in vivo. J Magn Reson Imaging. 2013; 38(3):511–529. [PubMed: 23722972]
6. Pipe JG, Zwart NR, Aboussouan EA, Robison RK, Devaraj A, Johnson KO. A new design and rationale for 3D orthogonally oversampled k-space trajectories. Magn Reson Med. 2011; 66(5): 1303–1311. [PubMed: 21469190]
7. Madelin G, Chang G, Otazo R, Jerschow A, Regatte RR. Compressed sensing sodium MRI of cartilage at 7T: preliminary study. J Magn Reson. 2012; 214(1):360–365. [PubMed: 22204825]
8. Madelin G, Kline R, Walvick R, Regatte RR. A method for estimating intracellular sodium concentration and extracellular volume fraction in brain in vivo using sodium magnetic resonance imaging. Sci Rep. 2014; 4:4763. [PubMed: 24755879]
9. Lu A, Atkinson IC, Claiborne TC, Damen FC, Thulborn KR. Quantitative sodium imaging with a flexible twisted projection pulse sequence. Magn Reson Med. 2010; 63(6):1583–1593. [PubMed: 20512862]
10. Boada FE, Gillen JS, Shen GX, Chang SY, Thulborn KR. Fast three dimensional sodium imaging. Magn Reson Med. 1997; 37(5):706–715. [PubMed: 9126944]
11. Nagel AM, Laun FB, Weber MA, Matthies C, Semmler W, Schad LR. Sodium MRI using a density-adapted 3D radial acquisition technique. Magn Reson Med. 2009; 62(6):1565–1573. [PubMed: 19859915]
12. Qian Y, Zhao T, Hue YK, Ibrahim TS, Boada FE. High-resolution spiral imaging on a whole-body 7T scanner with minimized image blurring. Magn Reson Med. 2010; 63(3):543–552. [PubMed: 20146226]
13. Shen GX, Boada FE, Thulborn KR. Dual-frequency, dual-quadrature, birdcage RF coil design with identical B1 pattern for sodium and proton imaging of the human brain at 1.5 T. Magn Reson Med. 1997; 38(5):717–725. [PubMed: 9358445]
14. Shen GX, Wu JF, Boada FE, Thulborn KR. Experimentally verified, theoretical design of dual-tuned, low-pass birdcage radiofrequency resonators for magnetic resonance imaging and magnetic resonance spectroscopy of human brain at 3.0 Tesla. Magn Reson Med. 1999; 41(2):268–275. [PubMed: 10080273]
15. Vaughan JT, Hetherington HP, Otu JO, Pan JW, Pohost GM. High frequency volume coils for clinical NMR imaging and spectroscopy. Magn Reson Med. 1994; 32(2):206–218. [PubMed: 7968443]
16. Xie, Z.; Xu, D.; Kelley, DA.; Vigneron, DB.; Zhang, X. Dual-frequency Volume Microstrip Coil with Quadrature Capability for 13C/1H MRI/MRS at 7T.. ISMRM Workshop on Advances in High Field MR; Pacific Grove, California, USA. 2007; Poster 41
17. Murphy-Boesch J, Srinivasan R, Carvajal L, Brown TR. Two configurations of the four-ring birdcage coil for 1H imaging and 1H-decoupled 31P spectroscopy of the human head. Journal of magnetic resonance Series B. 1994; 103(2):103–114. [PubMed: 8137076]

18. Amari S, Ulug AM, Bornemann J, van Zijl PC, Barker PB. Multiple tuning of birdcage resonators. Magn Reson Med. 1997; 37(2):243–251. [PubMed: 9001149]
19. Lanz T, von Kienlin M, Behr W, Haase A. Double-tuned four-ring birdcage resonators for in vivo 31P-nuclear magnetic resonance spectroscopy at 11.75 T. Magma. 1997; 5(3):243–246. [PubMed: 9351028]
20. Fitzsimmons JR, Beck BL, Brooker HR. Double resonant quadrature birdcage. Magn Reson Med. 1993; 30(1):107–114. [PubMed: 8396709]
21. Fleysher L, Oesingmann N, Brown R, Sodickson DK, Wiggins GC, Inglese M. Noninvasive quantification of intracellular sodium in human brain using ultrahigh-field MRI. NMR Biomed. 2013; 26(1):9–19. [PubMed: 22714793]
22. Adriany G, Gruetter R. A half-volume coil for efficient proton decoupling in humans at 4 tesla. J Magn Reson. 1997; 125(1):178–184. [PubMed: 9245377]
23. Schnall MD, Subramanian VH, Leigh JS, Chance B. A new double-tuned probe for concurrent 1H and 31P NMR. J Magn Reson. 1985; 65:122–129.
24. Bottomley PA, Hardy CJ, Roemer PB. Phosphate metabolite imaging and concentration measurements in human heart by nuclear magnetic resonance. Magn Reson Med. 1990; 14(3): 425–434. [PubMed: 2355826]
25. Bottomley PA, Hardy CJ, Roemer PB, Mueller OM. Proton-decoupled, Overhauser-enhanced, spatially localized carbon-13 spectroscopy in humans. Magn Reson Med. 1989; 12(3):348–363. [PubMed: 2560801]
26. Fitzsimmons JR, Brooker HR, Beck B. A transformer-coupled double-resonant probe for NMR imaging and spectroscopy. Magn Reson Med. 1987; 5(5):471–477. [PubMed: 3431409]
27. Fitzsimmons JR, Brooker HR, Beck B. A comparison of double-tuned surface coils. Magn Reson Med. 1989; 10(3):302–309. [PubMed: 2543881]
28. Klomp DW, van de Bank BL, Raaijmakers A, Korteweg MA, Possanzini C, Boer VO, van de Berg CA, van de Bosch MA, Luijten PR. 31P MRSI and 1H MRS at 7 T: initial results in human breast cancer. NMR Biomed. 2011; 24(10):1337–1342. [PubMed: 21433156]
29. Mispelter J, Tiffon B, Quiniou E, Lhoste JM. Optimization of 13C-1H double coplanar surface-coil design for WALTZ-16 decoupling sequence. JMR. 1989; 82:622–628.
30. Dabirzadeh A, McDougall MP. Trap Design for Insertable Second-Nuclei Radiofrequency Coils for Magnetic Resonance Imaging and Spectroscopy. Concepts in Magnetic Resonance Part B (Magnetic Resonance Engineering). 2009; 35B(3):121–132.
31. Avdievich NI, Hetherington HP. 4 T Actively detuneable double-tuned 1H/31P head volume coil and four-channel 31P phased array for human brain spectroscopy. J Magn Reson. 2007; 186(2): 341–346. [PubMed: 17379554]
32. Brown R, Madelin G, Lattanzi R, Chang G, Regatte RR, Sodickson DK, Wiggins GC. Design of a nested eight-channel sodium and four-channel proton coil for 7T knee imaging. Magn Reson Med. 2013; 70(1):259–268. [PubMed: 22887123]
33. Lakshmanan, K.; Brown, R.; Madelin, G.; Boada, FE.; Wiggins, G. An 8 Channel Transmit Receive Sodium & Nested 8 Channel Transmit Receive Proton Coil for 3.0 T Brain Imaging. ISMRM; Milan, Italy: 2014. p. 4879
34. Moon CH, Kim JH, Zhao T, Bae KT. Quantitative (23) Na MRI of human knee cartilage using dual-tuned (1) H/(23) Na transceiver array radiofrequency coil at 7 tesla. J Magn Reson Imaging. 2013; 38(5):1063–1072. [PubMed: 24123257]
35. Kaggie JD, Hadley JR, Badal J, Campbell JR, Park DJ, Parker DL, Morrell G, Newbould RD, Wood AF, Bangerter NK. A 3 T sodium and proton composite array breast coil. Magn Reson Med. 2014; 71(6):2231–2242. [PubMed: 24105740]
36. van der Velden TA, Italiaander M, van der Kemp WJ, Raaijmakers AJ, Schmitz AM, Luijten PR, Boer VO, Klomp DW. Radiofrequency configuration to facilitate bilateral breast 31P MR spectroscopic imaging and high-resolution MRI at 7 Tesla. Magn Reson Med. 2014
37. Shajan G, Mirkes C, Buckenmaier K, Hoffmann J, Pohmann R, Scheffler K. Three-layered radio frequency coil arrangement for sodium MRI of the human brain at 9.4 Tesla. Magn Reson Med. 2015

38. Reykowski, A. Theory and design of synthesis array coils for magnetic resonance imaging [PhD]. Texas A & M University; 1996.
39. Reykowski, A.; Wang, J. Rigid SNR analysis of coupled MRI coils connected to noisy preamplifiers and the effect of coil decoupling on combined SNR. ISMRM; Denver, CO: 2000. p. 1402
40. Scott, G. Preamplifier noise input coupling for phased arrays. ISMRM; Honolulu, Hawaii: 2002. p. 894
41. Findeklee C. Array Noise Matching—Generalization, Proof and Analogy to Power Matching. IEEE T Antennas and Propagation. 2011; 2:452–459.
42. Findeklee, C.; Duensing, R.; Reykowski, A. Simulating Array SNR & Effective Noise Figure in Dependance of Noise Coupling. ISMRM; Montreal, Canada: 2011. p. 1883
43. Vester, M.; Biber, S.; Rehner, R.; Wiggins, G.; Brown, R.; Sodickson, D. Mitigation of Inductive Coupling in Array Coils by Wideband Port Matching. ISMRM; Melbourne, Australia: 2012. p. 2690
44. Wiggins, GC.; Brown, R.; Zhang, B.; Vester, M.; Popescu, S.; Rehner, R.; Sodickson, D. SNR Degradation in Receive Arrays Due to Preamplifier Noise Coupling and a Method for Mitigation. ISMRM; Melbourne, Australia: 2012. p. 2689
45. Brown, R.; Lakshmanan, K.; Madelin, G.; Chang, G.; Sodickson, DK.; Regatte, RR.; Wiggins, GC. Design and Application of a Nested Multi-Channel Sodium Proton Knee Array at 3T. ISMRM; Milan, Italy: 2014. p. 4880
46. Kumar A, Edelstein WA, Bottomley PA. Noise figure limits for circular loop MR coils. Magn Reson Med. 2009; 61(5):1201–1209. [PubMed: 19253376]
47. Wiggins GC, Polimeni JR, Potthast A, Schmitt M, Alagappan V, Wald LL. 96-Channel receive-only head coil for 3 Tesla: design optimization and evaluation. Magn Reson Med. 2009; 62(3): 754–762. [PubMed: 19623621]
48. von Morze C, Tropp J, Banerjee S, Xu D, Karpodinis K, Carvajal L, Hess C, Mukherjee P, Majumdar S, Vigneron D. An eight-channel, nonoverlapping phased array coil with capacitive decoupling for parallel MRI at 3 T. Concepts in Magn Reson Part B. 2007; 31B(1):37–43.
49. Roemer PB, Edelstein WA, Hayes CE, Souza SP, Mueller OM. The NMR phased array. Magn Reson Med. 1990; 16(2):192–225. [PubMed: 2266841]
50. Lattanzi R, Grant AK, Polimeni JR, Ohliger MA, Wiggins GC, Wald LL, Sodickson DK. Performance evaluation of a 32-element head array with respect to the ultimate intrinsic SNR. NMR Biomed. 2010; 23(2):142–151. [PubMed: 19904727]
51. Schnell W, Renz W, Vester M, Ermert H. Ultimate Signal-to-Noise-Ratio of Surface and Body Antennas for Magnetic Resonance Imaging. IEEE T Antennas and Propagation. 2000; 48(3):418–428.
52. Wiggins, GC.; Brown, R.; Fleysher, L.; Zhang, B.; Stoeckel, B.; Inglese, M.; Sodickson, DK. A Nested Dual Frequency Birdcage/Stripline Coil for Sodium/Proton Brain Imaging at 7T. ISMRM; Stockholm, Sweden: 2010. p. 1500
53. Brown R, Deniz CM, Zhang B, Chang G, Sodickson DK, Wiggins GC. Design and application of combined 8-channel transmit and 10-channel receive arrays and radiofrequency shimming for 7-T shoulder magnetic resonance imaging. Invest Radiol. 2014; 49(1):35–47. [PubMed: 24056112]
54. Duan Q, Duyn JH, Gudino N, de Zwart JA, van Gelderen P, Sodickson DK, Brown R. Characterization of a dielectric phantom for high-field magnetic resonance imaging applications. Med Phys. 2014; 41(10):102303. [PubMed: 25281973]
55. Gabriel S, Lau RW, Gabriel C. The dielectric properties of biological tissues: II. Measurements in the frequency range 10 Hz to 20 GHz. Phys Med Biol. 1996; 41(11):2251–2269. [PubMed: 8938025]
56. Ishihara Y, Calderon A, Watanabe H, Okamoto K, Suzuki Y, Kuroda K. A precise and fast temperature mapping using water proton chemical shift. Magn Reson Med. 1995; 34(6):814–823. [PubMed: 8598808]
57. Tilley, AR. The measure of man and woman. The Whitney Library of Design; New York: 1993.

58. Finnerty, M.; Herczak, J.; Zheng, T.; Weaver, J.; Yang, X.; Fujita, H. A 3D Parallel Imaging Capable Transmit and 15-Channel Receive Array Knee Coil at 3T. ISMRM; Toronto, Canada: 2008. p. 1077

59. Kellman P, McVeigh ER. Image reconstruction in SNR units: a general method for SNR measurement. Magn Reson Med. 2005; 54(6):1439–1447. [PubMed: 16261576]

60. Fautz, HP.; Vogel, M.; Gross, P.; Kerr, A.; Zhu, Y. B1 mapping of coil arrays for parallel transmission. ISMRM; Toronto, Ontario: 2008. p. 1247

61. Sodickson, D.; Zhang, B.; Duan, Q.; Brown, R.; Lattanzi, R.; Lakshmanan, K.; Vaidya, M.; Yang, A.; Rehner, R.; Vester, M.; Popescu, S.; Biber, S.; Stoeckel, B.; Chang, H.; Wiggins, G. ISMRM; Milan, Italy: 2014. Is a “one size fits all” many-element bore-lining remote body array feasible for routine imaging?; p. 618

62. Mirkes CC, Hoffmann J, Shajan G, Pohmann R, Scheffler K. High-resolution quantitative sodium imaging at 9.4 tesla. Magn Reson Med. 2014

63. Atkinson IC, Lu A, Thulborn KR. Preserving the accuracy and resolution of the sodium bioscale from quantitative sodium MRI during intrasubject alignment across longitudinal studies. Magn Reson Med. 2012; 68(3):751–761. [PubMed: 22139900]

64. Jansen JF, Backes WH, Nicolay K, Kooi ME. 1H MR spectroscopy of the brain: absolute quantification of metabolites. Radiology. 2006; 240(2):318–332. [PubMed: 16864664]

65. Atkinson IC, Lu A, Thulborn KR. Clinically constrained optimization of flexTPI acquisition parameters for the tissue sodium concentration bioscale. Magn Reson Med. 2011; 66(4):1089–1099. [PubMed: 21446034]

66. Jost G, Harting I, Heiland S. Quantitative single-voxel spectroscopy: the reciprocity principle for receive-only head coils. J Magn Reson Imaging. 2005; 21(1):66–71. [PubMed: 15611950]

67. Klomp DW, Renema WK, van der Graaf M, de Galan BE, Kentgens AP, Heerschap A. Sensitivity-enhanced 13C MR spectroscopy of the human brain at 3 Tesla. Magn Reson Med. 2006; 55(2):271–278. [PubMed: 16372278]

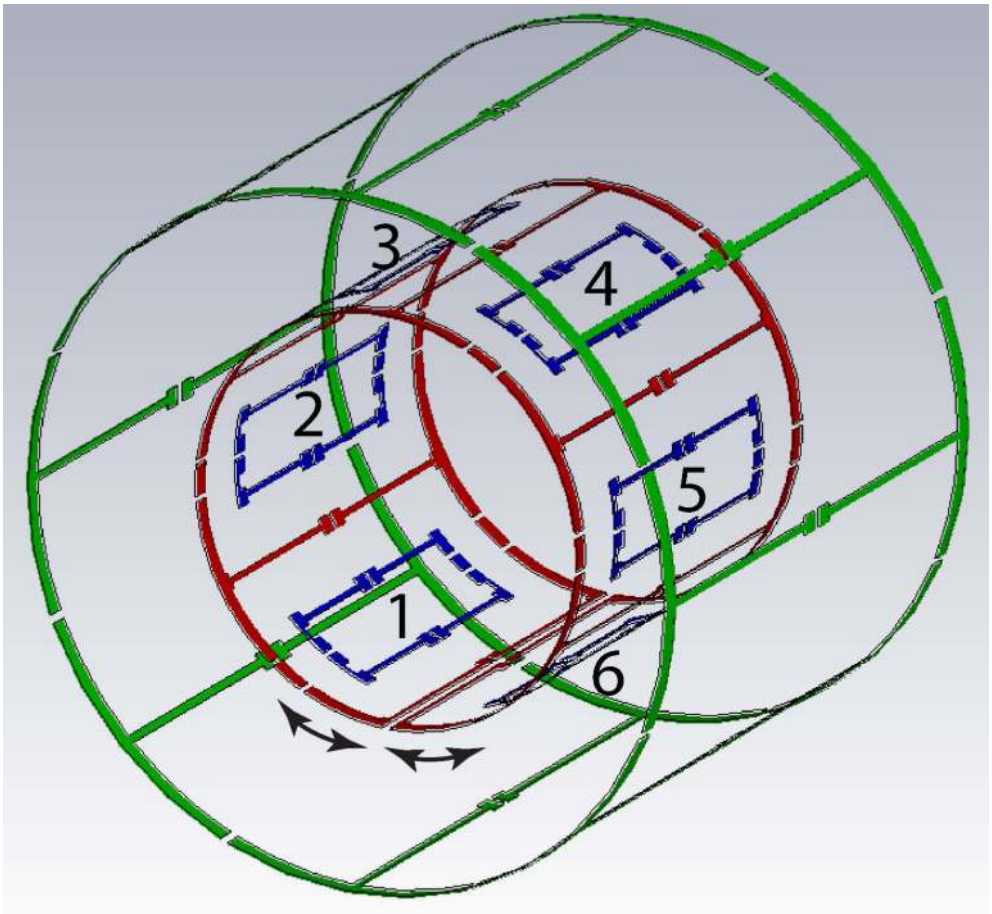

Figure 1.

Illustration of the developed 6×2 channel sodium/proton array that consists of three functional modules on two cylindrical layers. The flexible inner shell (15 cm diameter) houses the six channel sodium receive array (red) and six channel proton transceive array (blue). Paired concentric sodium/proton coil pairs are built on individual units linked with a hinge to the neighboring unit (see the photographs in Figure 2). Coil channel numbers are overlaid. Arrows between coils 1 and 6 indicate a discontinuity in the inner housing to allow patient entry. The rigid outer shell (25 cm diameter) houses the sodium birdcage (green), which is divisible into anterior and posterior halves for patient entry.

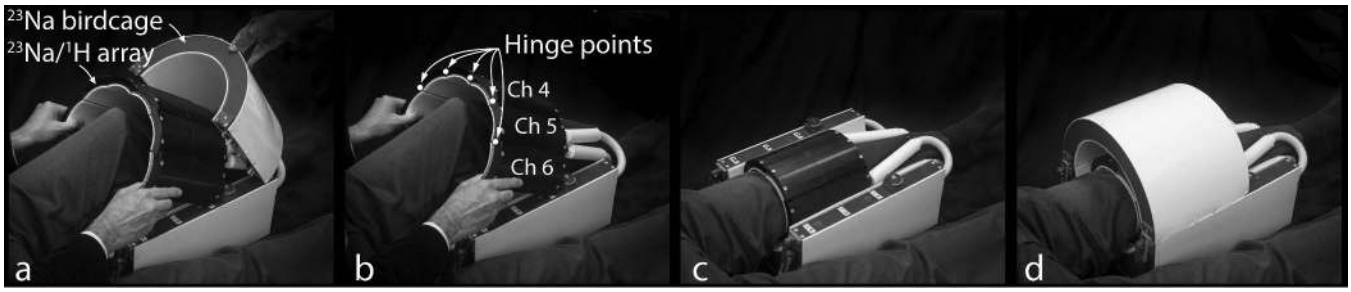

Figure 2.

Photographs of the sodium/proton knee array illustrate its modules and the patient positioning process: (a) the anterior half of the outer layer containing the sodium birdcage is separated from the posterior half and the flexible inner layer containing the sodium receive and proton transceive arrays is expanded while the patient's left knee is inserted, (b) six individual rigid units containing the sodium/proton arrays are outfitted with hinges to provide flexibility with the neighboring unit to combine the robustness of a rigid system with the sensitivity advantage of a tight-fitting flexible array, (c) the sodium/proton array is positioned around the patient, and (d) the anterior sodium birdcage is connected.

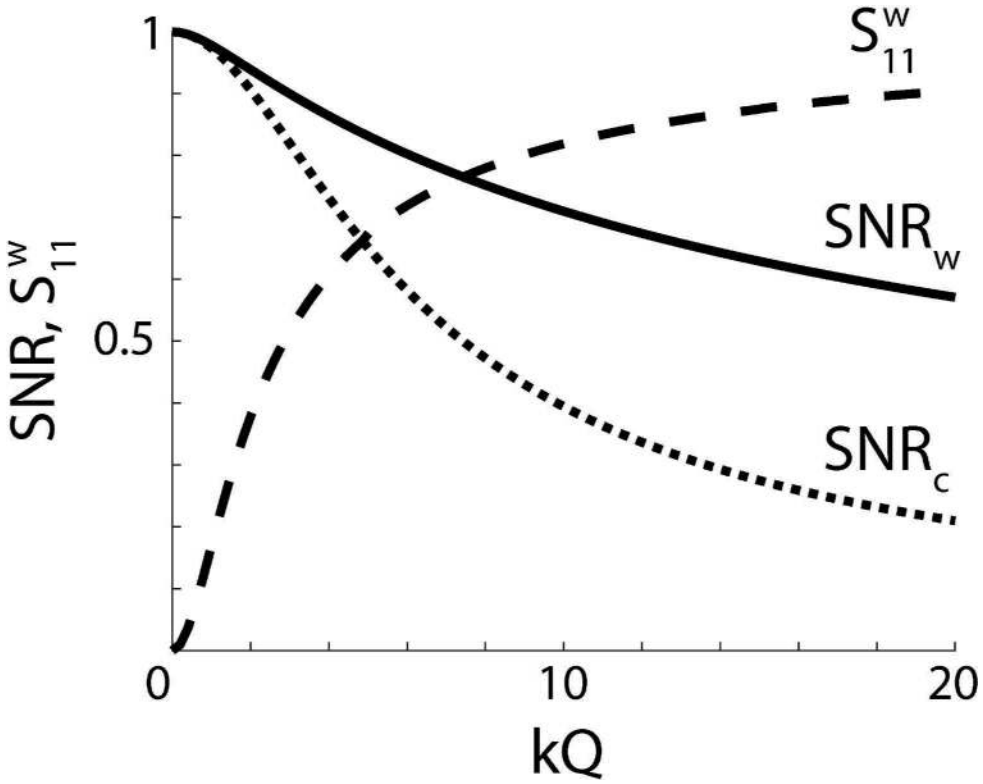

Figure 3.

Plot of the theoretical SNR of a coil element in a two-channel array, where unity represents that of an isolated coil (whose preamplifier noise factor is set to 1.122). SNR_w (solid line) is that predicted using the optimal wideband match, where the corresponding optimal wideband reflection coefficient is given by the S_{11}^{w} curve (long dashed line) for a range of kQ values. SNR_c (short dashed line) is that predicted using a classic match where $S_{11} = 0$. The plot shows that the wideband match scheme mitigates SNR degradation and provides substantial SNR gain over the classic strategy at high kQ values.

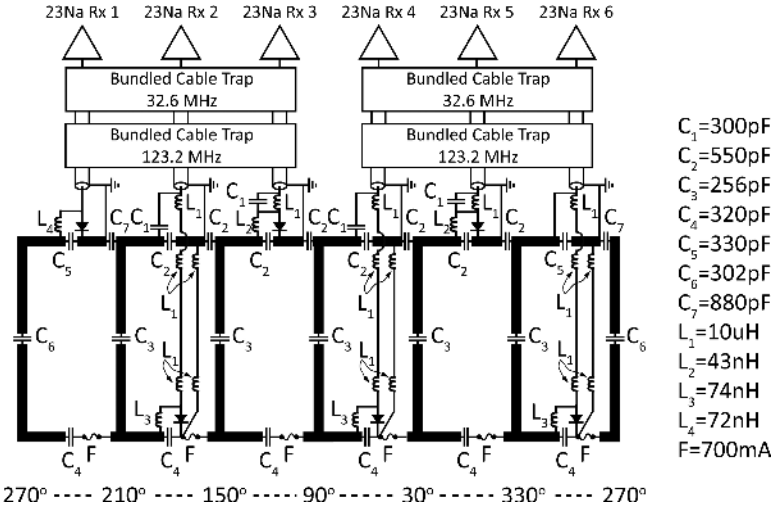

Figure 4.

Schematic diagram of the sodium receive array. Note that a parallel match capacitor (C_5) in channels 1 and 6 sets up a wideband match with $S_{11} = 0.86$, while a series match capacitor (C_1) in channels 2 to 4 sets up $S_{11} = 0.49$ (Smith Chart traces are shown in Figure 5). Azimuthal positions are indicated at the bottom (90° = anterior, 270° = posterior).

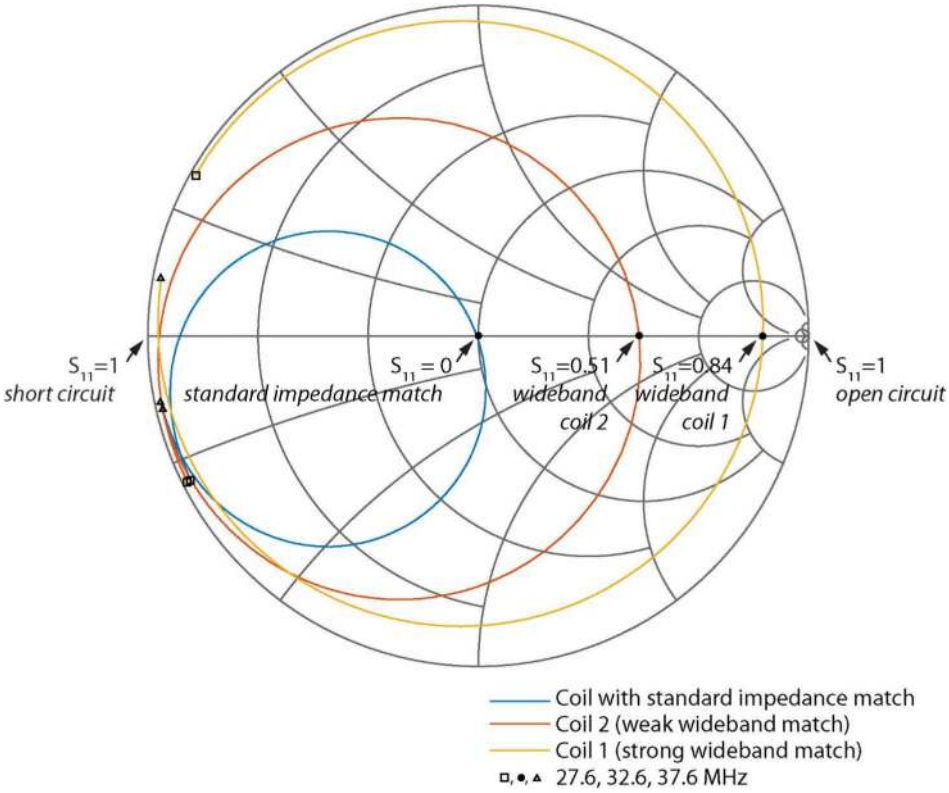

Figure 5.

Scattering parameter traces (S_{11}) for sodium receive coils matched to different reflection coefficients: standard 50 Ω match (blue), wideband match with S_{11} = 0.51 measured on coil 2 and applicable to coils 3-5 (red), and wideband match with S_{11}= 0.84 measured on coil 1 and applicable to coil 6 (gold). Traces are shown from 27.6 MHz (square markers) to 37.6 MHz (triangular markers) with the sodium resonance frequency (32.6 MHz) indicated by circular markers.

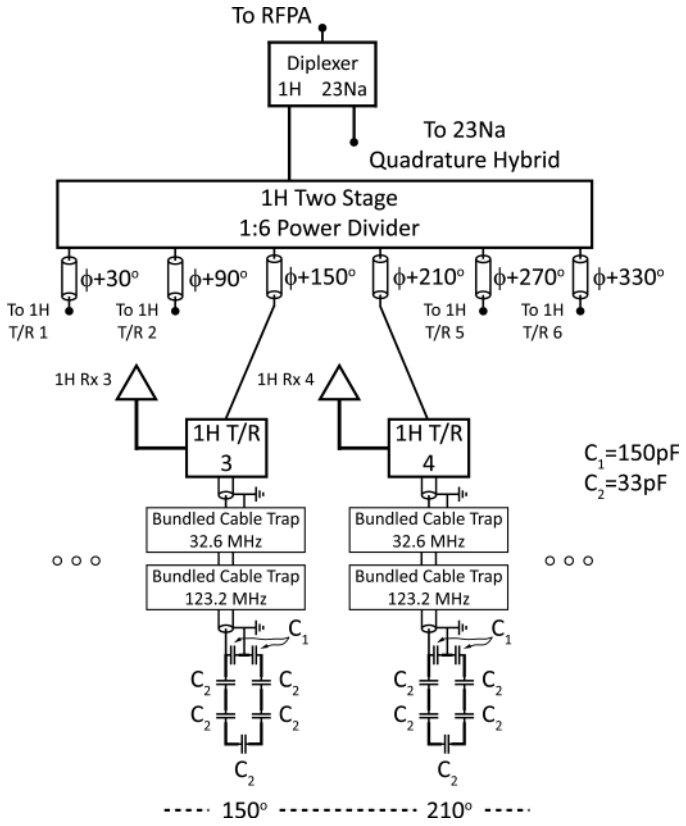

Figure 6.

Schematic diagram of the six-channel proton transmit/receive array. Azimuthal positions are indicated at the bottom (90° = anterior, 270° = posterior).

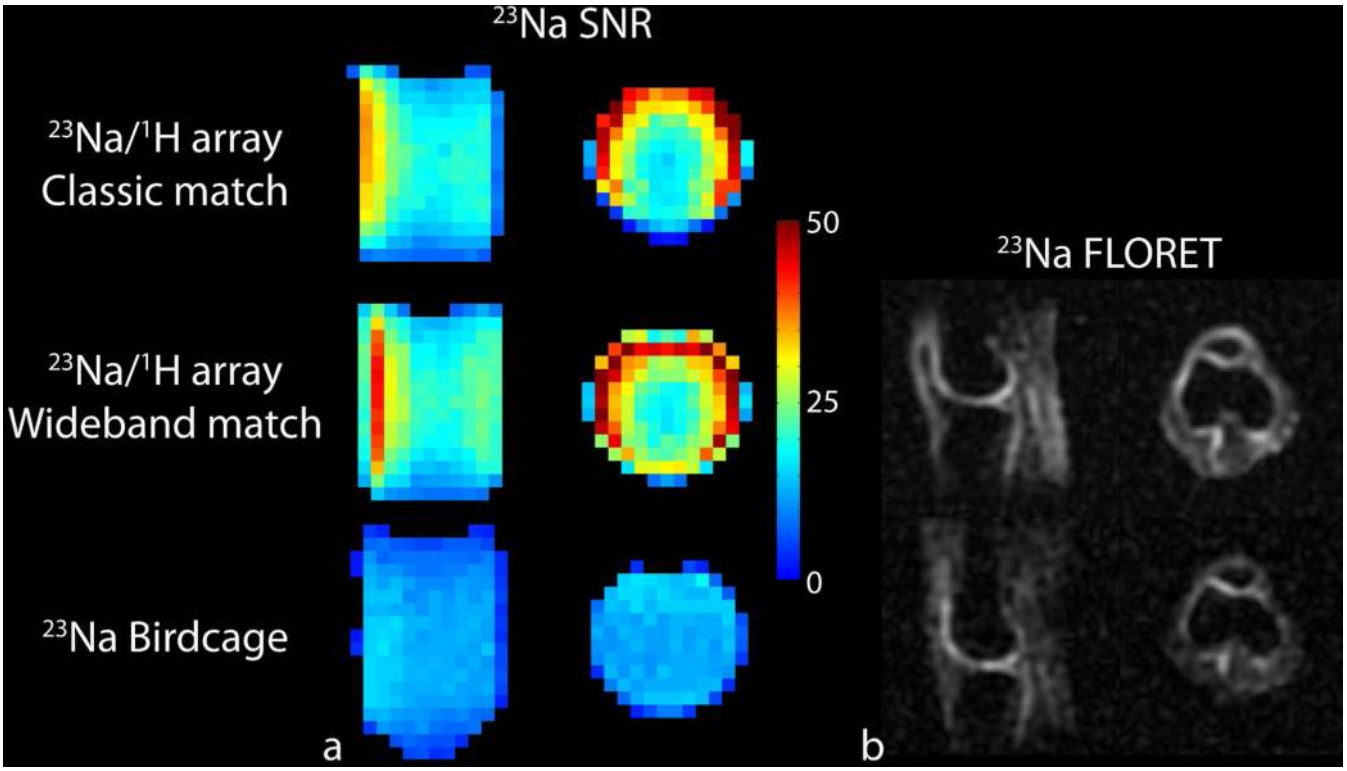

Figure 7.

Sodium coil performance comparison between the developed dual-nuclei array with classic 50 Ω matching (top row), wideband matching (middle row), and a conventional mono-nuclear sodium birdcage (bottom row). a) SNR measurements show the developed wideband-matched coil provided a 30% gain in the center and greater than two-fold in the periphery compared to the birdcage. The wideband match strategy provided a 50% SNR gain in the posterior portion of the phantom and 10% gain in the center compared to the conventional match. b) FLORET images of the knee and articular cartilage acquired with the developed array (top row) show qualitative advantages over those acquired with the sodium birdcage (bottom row).

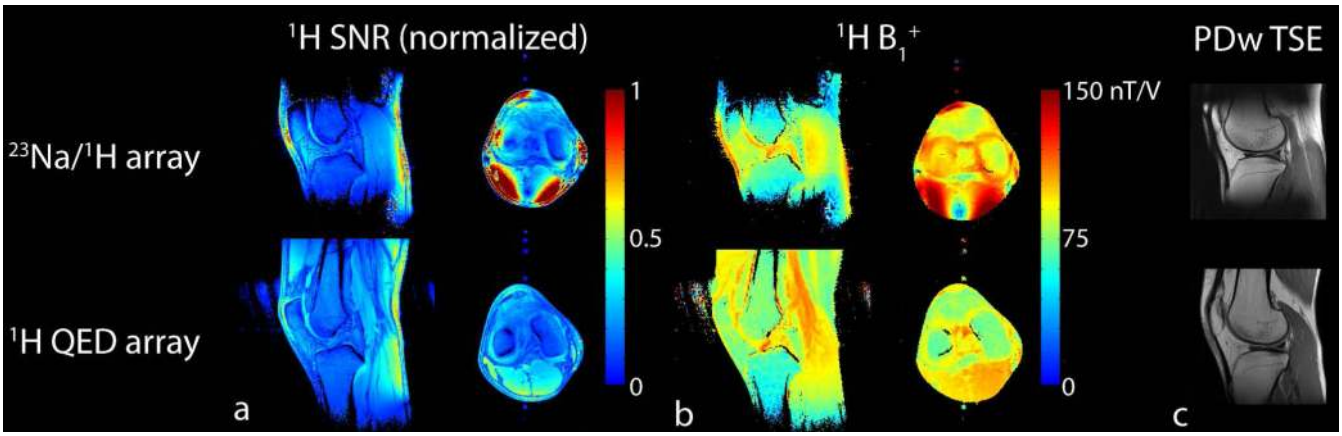

Figure 8.

Proton coil performance comparison between the developed dual-nuclei array (top row) and clinical 15-channel proton array by QED (bottom row): a) SNR, b) flip angle distribution, and c) anatomical image.

Table 1

Pulse sequence parameters.

Description	**B_1^+ mapping**		**SNR measurement**		**Anatomical**	**Metabolic**
Pulse sequence	**2D GRE**		**2D GRE**		**2D PDw FSE***	**3D FLORET****
Nucleus	**^{23}Na**	**^{1}H**	**^{23}Na**	**^{1}H**	**^{1}H**	**^{23}Na**
Voxel size (mm^3)	10.4×10.4×50.0	1.5×1.5×5.0	10.4×10.4×50	0.9×0.9×3.0	0.4×0.4×3.0	4.0×4.0×4.0
TE (ms)	3.1	2.4	3.1	4.1	29	0.2
TR (ms)	200	1000	200	200	3000	80
Flip angle (°)	-	-	90	20	90 (excitation) 156 (refocusing)	80
Bandwidth (Hz/pixel)	300	651	300	300	401	-
Number of slices	1	1	1	1	29	64
Field-of-view (mm^2)	500×500	192×192	500×500	220×220	140×140	256×256
Acquisition time (s)	11	8	11	53	204	864

*A turbo factor of five and parallel imaging acceleration factor of two was applied to the fast spin echo acquisition.

**Other relevant parameters were: 3 hubs at 45°, 300 interleaves per hub, 12 averages, ADC duration = 6.25 ms, and dwell time = 10 us.